

HYSTERESIS BETWEEN DISTINCT MODES OF TURBULENT DYNAMOS

BIDYA BINAY KARAK¹, LEONID L. KITCHATINOV^{2,3}, AXEL BRANDENBURG^{1,4}

¹Nordita, KTH Royal Institute of Technology and Stockholm University, Roslagstullsbacken 23, SE-10691 Stockholm, Sweden

²Institute of Solar-Terrestrial Physics, PO Box 291, Irkutsk 664033, Russia

³Pulkovo Astronomical Observatory, St. Petersburg, 196140, Russia

⁴Department of Astronomy, Stockholm University, SE-10691 Stockholm, Sweden

Draft version November 4, 2014

ABSTRACT

Nonlinear mean-field models for the solar dynamo show long-term variability, which may be relevant to different states of activity inferred from long-term radiocarbon data. This paper is aimed to probe the dynamo hysteresis predicted by the recent mean-field models of Kitchatinov & Olemskoy (2010) with direct numerical simulations. We perform three-dimensional simulations of large-scale dynamos in a shearing box with helically forced turbulence. As initial condition, we either take a weak random magnetic field or we start from a snapshot of an earlier simulation. Two quasi-stable states are found to coexist in a certain range of parameters close to onset of the large-scale dynamo. The simulations converge to one of these states in dependence on the initial conditions. When either the fractional helicity or the magnetic Prandtl number is increased between successive runs above the critical value for onset of the dynamo, the field strength jumps to a finite value. However, when the fractional helicity or the magnetic Prandtl number is then decreased again, the field strength stays at a similar value (strong field branch) even below the original onset. We also observe intermittent decaying phases away from the strong field branch close to the point where large-scale dynamo action is just possible. The dynamo hysteresis seen previously in mean-field models is thus reproduced by 3D simulations. Its possible relation to distinct modes of solar activity such as grand minima is discussed.

Subject headings: dynamo – magnetohydrodynamics (MHD) – turbulence – Sun: magnetic fields – Sun: activity

1. INTRODUCTION

The solar magnetic activity cycle is not a strictly periodic phenomenon. Its duration and strength vary from cycle to cycle. An impressive example of this aperiodicity is the famous Maunder minimum when sunspots were extremely scarce over about 70 years (Hoyt & Schatten 1996). The prolonged events of low magnetic activity like the Maunder minimum are typical characteristics of the Sun. Radiocarbon data reveal solar activity variations for the past $\sim 11,000$ years with 27 grand minima covering about 17% of time (Usoskin et al. 2007).

Dynamo theory for solar activity explains the grand minima by fluctuations in dynamo parameters (e.g., Choudhuri 1992; Ossendrijver et al. 1996; Charbonneau et al. 2004; Brandenburg & Spiegel 2008; Moss et al. 2008; Choudhuri & Karak 2009; Passos et al. 2014) or the meridional circulation (Karak 2010). The fluctuations cause irregular changes of dynamo cycle amplitudes with occasional wandering into states of low cycles strength. Dynamo models with fluctuating parameters generally reproduce the grand minima statistics (e.g., Choudhuri & Karak 2012; Karak & Choudhuri 2013; Olemskoy & Kitchatinov 2013). Recent analysis of radiocarbon data by Usoskin et al. (2014), however, showed that grand minima do not constitute a low-activity tail of the distribution common for all activity cycles, but represent a separate activity mode that cannot be interpreted as a fluctuation of the ‘regular’ mode. They concluded that solar dynamo regimes in grand min-

ima and in regular cycles are distinct.

The difference in dynamo operation between grand minima and regular activity modes can be interpreted as a consequence of a hysteresis phenomenon found in nonlinear mean-field dynamo models (Kitchatinov & Olemskoy 2010). The majority of such models for the solar dynamo employ suppression of poloidal field generation by the magnetic field (α -quenching). This nonlinearity serves well for stabilizing magnetic field growth. The dynamo-amplification of magnetic field takes place when the dynamo number

$$\mathcal{D} = \frac{\alpha \Delta \Omega R_{\odot}^3}{\eta_T} \quad (1)$$

exceeds a critical value \mathcal{D}_c , where $\eta_T = \eta + \eta_t$ is the total (microphysical plus turbulent) magnetic diffusivity, $\Delta \Omega$ is the angular velocity variation in the Sun, and α is the measure of the α -effect; see Krause & Rädler (1980). A decrease of α with increasing magnetic field strength reduces the effective dynamo number to saturate the field growth.

However, not only α but also the eddy diffusivity η_t is magnetically quenched. Using predictions of quasi-linear theory for α - and η_t -quenching results in a non-monotonous dependence of the effective (magnetically modified) dynamo-number on the magnetic field (see Fig. 1 in Kitchatinov & Olemskoy 2010). This number initially *increases* with magnetic field but the dependence changes to a decrease for stronger fields. If the dynamo number (1) is increased from a subcritical value, the saturated field amplitude jumps to a finite value of the or-

der of the equipartition field just after \mathcal{D} exceeds \mathcal{D}_c and then varies smoothly with increasing \mathcal{D} (Rüdiger et al. 1994). If the dynamo number is then decreased, dynamo-generated finite fields survive for $\mathcal{D} < \mathcal{D}_c$, but for sufficiently small values of \mathcal{D} , the field eventually falls to zero. The saturated field amplitude, therefore, depends on the pre-history of the \mathcal{D} variation (the dynamo hysteresis). In a finite range of \mathcal{D} -values, there are two stable solutions with considerably different characteristic strengths of magnetic field. Fluctuations in dynamo parameters provoke irregular transitions between these two solutions (Kitchatinov & Olemskoy 2010). The dynamo hysteresis can thus explain the distinction between grand minima and regular activity modes found by Usoskin et al. (2014).

Kitchatinov & Olemskoy (2010) used a mean-field dynamo model which cannot be free from arbitrary prescriptions. Apart from magnetic quenching of α and η_t , there are other nonlinearities which all are implicitly present in direct numerical simulations (DNS). This paper probes the dynamo hysteresis with DNS. Using a shearing box setup, we perform simulations of helically forced turbulence, which produce oscillating (solar-type) dynamos. Ideally, this should be studied in realistic global rotating magneto-convection simulations in spherical geometry. However, at present, these simulations are premature and still far from realistic solar conditions (e.g., Nelson et al. 2013; Karak et al. 2014). By varying the amount of relative kinetic helicity, the hysteresis-type dependence of the oscillation amplitude on the pre-history of helicity variations is clearly seen. Similar behavior is also found when magnetic diffusion is varied. The simulations generally confirm the presence of two distinct regimes of large-scale dynamos in the vicinity of the dynamo threshold.

We note that turbulent large-scale dynamos near onset have already been studied by Rempel et al. (2009), who used ABC flow forcing. They found intermittent large-scale fields right after dynamo onset, but in their case no cyclic dynamos where possible nor did they find evidence of two distinct states.

2. THE MODEL SETUP

In our model, we assume the fluid to be isothermal and compressible. It obeys the equation of state $p = c_s^2 \rho$, with constant sound speed c_s . Hence we solve the following equations:

$$\frac{D\mathbf{U}}{Dt} = -SU_x\hat{y} - c_s^2 \nabla \ln \rho + \rho^{-1}(\mathbf{J} \times \mathbf{B} + \nabla 2\rho\nu\mathbf{S}) + \mathbf{f}, \quad (2)$$

$$\frac{D \ln \rho}{Dt} = -\nabla \cdot \mathbf{U}, \quad (3)$$

$$\frac{\partial \mathbf{A}}{\partial t} + \overline{\mathbf{U}}^{(S)} \cdot \nabla \mathbf{A} = -SA_y\hat{x} + \mathbf{U} \times \mathbf{B} + \eta \nabla^2 \mathbf{A}. \quad (4)$$

Here $D/Dt = \partial/\partial t + (\mathbf{U} + \overline{\mathbf{U}}^{(S)}) \cdot \nabla$ is the advective time derivative, $\overline{\mathbf{U}}^{(S)} = (0, Sx, 0)$ with $S = \text{const}$ is the imposed uniform large-scale shear flow, ν is the constant kinematic viscosity, \mathbf{A} is the magnetic vector potential, $\mathbf{B} = \nabla \times \mathbf{A}$ is the magnetic field, $\mathbf{J} = \mu_0^{-1} \nabla \times \mathbf{B}$ is the current density, η is the constant microscopic diffusivity, and \mathbf{f} is a forcing function to be specified below. The traceless rate of strain tensor \mathbf{S} is given by

$\mathbf{S}_{ij} = \frac{1}{2}(U_{i,j} + U_{j,i}) - \frac{1}{3}\delta_{ij}\nabla \cdot \mathbf{U}$, where the commas denote partial differentiation with respect to the coordinate (j or i).

Turbulence is sustained by supplying energy to the system through a forcing function $\mathbf{f} = \mathbf{f}(\mathbf{x}, t)$, which is helical and random in time (δ -correlated). It is defined as

$$\mathbf{f}(\mathbf{x}, t) = \text{Re}\{N\mathbf{f}_{\mathbf{k}(t)} \exp[i\mathbf{k}(t) \cdot \mathbf{x} + i\phi(t)]\}, \quad (5)$$

where \mathbf{x} is the position vector. At each timestep the wavevector $\mathbf{k}(t)$ randomly takes any value from many possible wavevectors in a certain range around a given forcing wavenumber k_f . The phase $-\pi < \phi(t) \leq \pi$ also changes randomly at every timestep. On dimensional grounds, we choose $N = f_0 c_s (|\mathbf{k}| c_s / \delta t)^{1/2}$, where f_0 is a non-dimensional forcing amplitude. The transverse helical waves are produced via Fourier amplitudes (Haugen et al. 2004)

$$\mathbf{f}_{\mathbf{k}} = \mathbf{R} \cdot \mathbf{f}_{\mathbf{k}}^{(\text{nohel})} \quad \text{with} \quad R_{ij} = \frac{\delta_{ij} - i\sigma\epsilon_{ijk}\hat{k}_k}{\sqrt{1 + \sigma^2}}, \quad (6)$$

where σ is a measure of the helicity of the forcing; for positive maximum helicity $\sigma = 1$. The nonhelical forcing function, $\mathbf{f}_{\mathbf{k}}^{(\text{nohel})} = (\mathbf{k} \times \hat{\mathbf{e}}) / \sqrt{\mathbf{k}^2 - (\mathbf{k} \cdot \hat{\mathbf{e}})^2}$, where $\hat{\mathbf{e}}$ is an arbitrary unit vector not aligned with \mathbf{k} . Note that $|\mathbf{f}_{\mathbf{k}}|^2 = 1$ and $\mathbf{f}_{\mathbf{k}} \cdot (i\mathbf{k} \times \mathbf{f}_{\mathbf{k}})^* = 2\sigma k / (1 + \sigma^2)$.

The fluid and magnetic Reynolds numbers, and the magnetic Prandtl number are defined as

$$\text{Re} = u_{\text{rms}}/\nu k_f, \quad R_m = u_{\text{rms}}/\eta k_f, \quad P_m = \nu/\eta, \quad (7)$$

where $u_{\text{rms}} = \langle \mathbf{u}^2 \rangle^{1/2}$ is the rms value of the velocity in the statistically stationary state with $\langle \cdot \rangle$ denoting the average over the whole domain and k_f is the mean forcing wavenumber.

The boundary conditions are shearing-periodic in the x direction, and periodic in the y and z directions with dimensions $L_x = L_y = L_z = 2\pi$. We always choose $S = -0.2$, $f_0 = 0.01$ and $k_f = 5k_1$ or $3k_1$, where $k_1 = 2\pi/L_x = 1$ is the smallest possible wavenumber of the box. We use non-dimensional units by setting $c_s = \rho_0 = \mu_0 = 1$, where $\rho_0 = \langle \rho \rangle$ is the volume-averaged density, which is constant in time. As initial conditions we take $\mathbf{u} = \ln \rho = 0$ and a small-scale low amplitude (10^{-4}) Gaussian noise for \mathbf{A} . All computations are performed using the PENCIL CODE¹. The grid resolution of all runs presented in this paper is 96^3 .

3. RESULTS

We begin by focusing on the following two sets of simulations. In one, we have simulations for different helicity of the forcing by taking weak fields as initial conditions (described in §2). These simulations are performed to identify the onset of the dynamo. In the other set, we take as initial conditions a snapshot of a previous simulation right after onset of the dynamo which produces an oscillatory dynamo solution. We perform several simulations by successively reducing the helicity by a small value and using the resulting fields of the previous simulation as the initial condition. We continue this procedure until there is only a decaying solution. In this

¹ <http://pencil-code.googlecode.com>

way we identify the regime of dynamo hysteresis as the location where, depending on the initial conditions, both non-decaying oscillatory dynamos and decaying solutions are possible, i.e., the system becomes bistable. Finally we repeat the whole procedure in a different parameter regime and explore the robustness of the results.

3.1. Onset of dynamo action

We perform several simulations by increasing the strength of helicity parameter σ of the turbulent forcing, starting from 0 to 1 (Set I). For this set we fix $\eta = \nu = 0.005$ and $k_f = 5k_1$. Runs A–M in Table 1 show these simulations. Along with other important parameters we show a rough measure of the dynamo number defined as $D = C_\alpha C_\Omega$, where $C_\alpha = \alpha_0/\eta_T k_1$, and $C_\Omega = |S|/\eta_T k_1^2$, with $\alpha_0 = -\frac{1}{3}\tau\langle\boldsymbol{\omega} \cdot \mathbf{u}\rangle$, $\tau = (u_{\text{rms}} k_f)^{-1}$, $\eta_T = \eta + \eta_{\text{to}}$ and $\eta_{\text{to}} = \frac{1}{3}\tau\langle\mathbf{u}^2\rangle$. In Figure 1 we show the temporal mean in the statistically stationary state of the large-scale magnetic field over the whole domain $\bar{B}_{\text{rms}} = (\langle B_x \rangle_y^2 + \langle B_y \rangle_y^2 + \langle B_z \rangle_y^2)^{1/2}$ normalized by $B_{\text{eq}} = u_{\text{rms}}$. We see that the large-scale field is zero when σ is below about 0.32, implying there is no dynamo action. For $\sigma = 0.32$ (Run D) in Figure 2 we show the spatio-temporal variation of the y -component of the mean magnetic field $\bar{B}_y = \langle B_y \rangle_{xy}$ (which corresponds to the toroidal field in spherical coordinates) and the time series of \bar{B}_y^2 at an arbitrarily chosen mesh point, normalized by B_{eq}^2 (which may be considered as a measure of sunspot number). Here we do not see clear magnetic oscillations. A few cycles started to appear at around $t = 2$, but they did not survive. The overall field is also very weak. On increasing σ slightly we observe dynamo transition at $\sigma = 0.322$ (Run E) and the magnetic field becomes strong ($\bar{B}_{\text{rms}} > B_{\text{eq}}$). Hence the critical value of σ for dynamo action is $\sigma_c \approx 0.322$. The spatio-temporal variation for this case is shown in Figure 3 where we see clear magnetic cycles with the dynamo wave propagation along positive z direction. Together with positive helicity (which makes negative α) and negative shear, this is indeed expected. However, the cycles are not regular; the amplitude varies from cycle to cycle similar to the observed solar cycle. This cycle irregularity is related to the scale-separation ratio which has been demonstrated in Brandenburg & Guerrero (2012). For $\sigma > \sigma_c$ we always observe clear magnetic cycles and the value of \bar{B}_{rms} remains around B_{eq} ; see Figure 1.

3.2. Dynamo hysteresis

Now we take a snapshot of a simulation at $\sigma = \sigma_c = 0.322$ (Run E which is shown in Figure 3) and perform a set of simulations by reducing σ slowly and taking the output of the previous simulation as initial conditions. Runs E1–E12 in Table 1 represent such cases and the corresponding \bar{B}_{rms} are shown in Figure 1 as red diamonds. We observe oscillatory solutions over a broad parameter range: $0.22 \leq \sigma < 0.322$, in which there are otherwise decaying solutions when started from weak fields. Therefore, in this range, the results depend on the initial condition, i.e., system becomes bistable. All the simulations are run for sufficiently long time to ensure that they remain in the same state. In Figure 4 we show

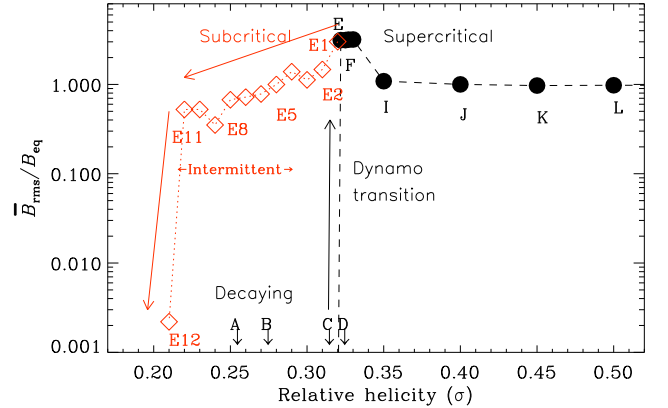


FIG. 1.— Dynamo hysteresis, as seen in the mean large-scale magnetic field as a function of σ (Set I). The filled circles and the red diamonds are from simulations which started with weak random seed fields (Runs A–M; arrows denote the zero values for Runs A–D) and strong oscillatory fields of the previous simulation (Runs E1–E12), respectively. Runs E5–E11 show intermittent behavior.

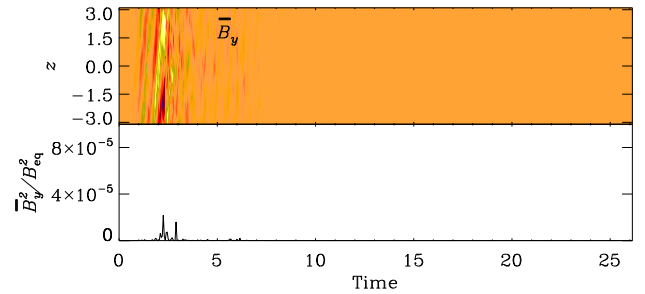


FIG. 2.— Top: the y component of mean magnetic field \bar{B}_y and bottom: its time series at an arbitrarily chosen mesh point as a function of time, normalized by the diffusive time $(k_1^2 \eta)^{-1}$. These results are from a simulation started with weak seed field at $\sigma = 0.32$, which is just before the onset of dynamo action (Run D).

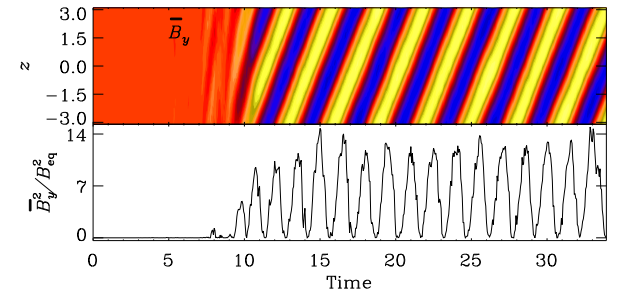


FIG. 3.— Results from the simulation started from weak seed field at $\sigma = 0.322$, which is just right after the dynamo transition (Run E). The format is the same as Figure 2.

the magnetic oscillations from the last run (Run E11) at $\sigma = 0.22$, below which the oscillations die completely. We see that the magnetic cycles persist most of the time in this simulation. The interesting feature is that occasionally some of the cycles disappear or become weaker. By comparing the first two panels of Figure 4 we notice that during weaker cycles (for example, time ~ 130 , 154), \bar{B}_x is not reduced as much as \bar{B}_y , implying that the α effect dominates over the Ω effect. This kind of intermittent behavior closely resembles the grand minima observed in Sun. We see a similar behavior for many

TABLE 1
SUMMARY OF THE RUNS.

Set I								Set II									
Run	σ	u_{rms}	R_m	D	\bar{B}	\bar{B}_x	\bar{B}_y	Osc	Run	P_m	u_{rms}	R_m	D	\bar{B}	\bar{B}_x	\bar{B}_y	Osc
A	0.25	0.32	12.7	3.28	0.00	0.00	0.00	N	N	0.062	0.23	0.6	0.80	0.00	0.00	0.00	N
B	0.27	0.30	11.9	4.10	0.00	0.00	0.00	N	O	0.100	0.34	1.3	0.86	0.00	0.00	0.00	N
C	0.31	0.35	13.6	3.33	0.00	0.00	0.00	N	P	0.167	0.28	1.8	2.49	0.00	0.00	0.00	N
D	0.32	0.32	12.5	4.26	0.00	0.00	0.00	N	Q	0.250	0.31	3.1	3.07	0.00	0.00	0.00	N
E	0.322	0.12	4.8	22.0	3.14	0.21	3.08	Y	R	0.263	0.27	2.8	4.35	0.00	0.00	0.00	N
F	0.325	0.12	4.9	22.1	3.14	0.21	3.09	Y	S	0.278	0.25	2.7	5.57	0.00	0.00	0.00	N
G	0.327	0.12	4.8	22.7	3.17	0.21	3.16	Y	T	0.294	0.16	1.8	6.70	1.68	0.23	1.59	Y
H	0.33	0.12	4.8	23.0	3.19	0.21	3.14	Y	U	0.312	0.18	2.3	5.21	1.51	0.20	1.48	Y
I	0.35	0.21	8.3	7.31	1.09	0.18	0.93	Y	V	0.357	0.19	2.6	5.74	1.66	0.22	1.75	Y
J	0.40	0.22	8.6	7.47	1.00	0.20	0.76	Y	W	0.500	0.19	3.8	7.18	2.03	0.29	2.93	Y
K	0.45	0.22	8.7	7.79	0.97	0.21	0.73	Y	X	0.556	0.23	5.0	6.14	1.12	0.22	0.93	Y
L	0.50	0.23	8.9	7.89	0.98	0.22	0.71	Y	Y	0.625	0.23	5.8	6.51	1.05	0.23	0.81	Y
M	1.00	0.23	9.1	9.14	0.97	0.27	0.64	Y	Z	0.714	0.24	6.7	6.69	1.03	0.23	0.87	Y
E1	0.32	0.13	5.0	20.0	3.01	0.20	2.96	Y	T1	0.278	0.13	1.4	8.52	1.92	0.29	1.88	Y
E2	0.31	0.24	9.6	4.88	1.47	0.10	1.43	Y	T2	0.250	0.13	1.3	7.45	1.69	0.27	1.65	Y
E3	0.30	0.28	11.2	3.30	1.13	0.09	1.06	Y	T3	0.200	0.13	1.0	6.25	1.34	0.26	1.29	Y
E4	0.29	0.25	10.0	4.16	1.39	0.10	1.37	Y	T4	0.179	0.14	1.0	5.29	1.10	0.23	1.04	Y
E5	0.28	0.30	11.9	2.74	1.00	0.08	0.93	Int	T5	0.167	0.15	1.0	4.54	0.92	0.20	0.86	Y
E6	0.27	0.34	13.4	2.12	0.78	0.07	0.72	Int	T6	0.161	0.15	0.9	4.43	0.88	0.20	0.82	Y
E7	0.26	0.36	13.9	1.91	0.72	0.06	0.66	Int	T7	0.156	0.33	2.0	1.60	0.00	0.00	0.00	N
E8	0.25	0.37	14.7	1.77	0.67	0.06	0.63	Int	T8	0.154	0.35	2.1	1.44	0.00	0.00	0.00	N
E9	0.24	0.34	14.6	1.97	0.35	0.04	0.29	Int	T9	0.152	0.32	1.9	1.71	0.00	0.00	0.00	N
E10	0.23	0.33	12.8	2.36	0.52	0.05	0.45	Int	T10	0.147	0.21	1.2	3.25	0.00	0.00	0.00	N
E11	0.22	0.28	11.0	3.17	0.52	0.05	0.43	Int	T11	0.143	0.39	2.2	1.06	0.00	0.00	0.00	N
E12	0.21	0.32	12.5	2.93	0.00	0.00	0.00	Y	T12	0.132	0.31	1.6	1.47	0.00	0.00	0.00	N

NOTE. — Runs A–E12 belong to Set I in which σ is varied. Runs A–M are started from weak seed fields. Run E1 is performed from a snapshot of Run E (highlighted), but at slightly reduced σ . A similar procedure is continued from Runs E1 → E2 → E3 ... → E12. Runs N–T12 belong to Set II in which P_m is varied. Runs N–Z are started from weak seed fields. Run T1 is started from a snapshot of Run T (highlighted), but at decreased P_m , and a similar procedure is performed for Runs T1 → T2 → T3 ... → T12. $\bar{B} = \bar{B}_{\text{rms}}/B_{\text{eq}}$, $\tilde{B}_x = \langle \bar{B}_x^2 \rangle^{1/2}/B_{\text{eq}}$, and $\tilde{B}_y = \langle \bar{B}_y^2 \rangle^{1/2}/B_{\text{eq}}$. The columns ‘Osc’ indicate whether there are oscillations (Y) or not (N) and ‘Int’ denotes intermittent behavior.

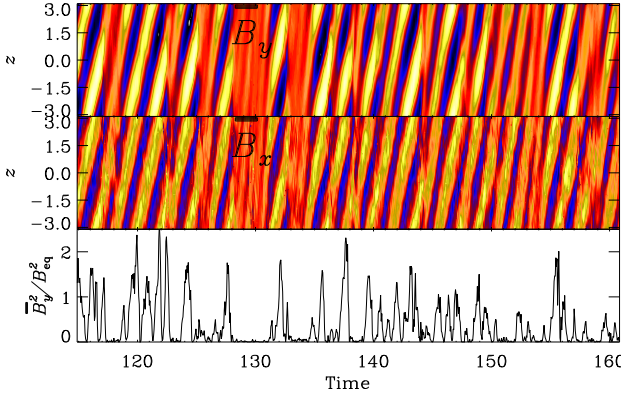


FIG. 4.— In the bistable dynamo state of Figure 1: The simulation started from strong initial field at $\sigma = 0.22$, just before the decaying solution (Run E11). The format is the same as Figure 2, but here the x component of \bar{B}_x is also displayed in the middle panel.

runs in the bistable region, particularly in Runs E5–E11.

3.3. Dynamo hysteresis: dependence on P_m

To explore the robustness of the existence of dynamo hysteresis, we repeat the same procedure in different parameter regimes of the simulations. Here we fix σ at 1 (fully helical flow) but vary the magnetic diffusivity η in each simulation; see Runs N–Z of Set II in Table 1.

Hence, P_m varies, but $\nu = 0.005$ is unchanged. This is similar to the experiments of Rempel et al. (2009), who used ABC flow forcing.

The black points in Figure 5 show \bar{B}_{rms} from different simulations started with weak seed fields as the initial conditions (Runs N–Z). We see that when P_m just exceeds about 0.29, the dynamo is excited and the magnetic field becomes oscillatory. The critical P_m for dynamo action is $P_m^c \approx 0.294$.

Next, as before, we take an oscillatory dynamo solution (Run T) as initial condition for the new simulation and decrease P_m by a small value progressively in each simulation by taking as initial conditions the last snapshot from the previous simulation. Runs T1–T12 in Table 1 are such examples and the corresponding \bar{B}_{rms} are shown as red diamonds in Figure 5. We see that, up to about $P_m = 0.16$, we obtain an oscillatory large-scale magnetic field. Figure 6 shows the typical magnetic cycles from a simulation at $P_m = 0.1613$ (Run T6) below which the oscillation dies. Note that in the bistable stage, unlike in previous set of simulations, for example shown in Figure 4 where some of the magnetic cycles disappear occasionally, here we observe cycles all the time. However when we repeat the whole procedure at $\sigma = 0.5$ instead of 1, we see this kind of intermittent behavior in the bistable regime. To obtain even more confidence in the results we have repeated another set of simulations (Set III) at $k_f = 3$ and $\nu = 8 \times 10^{-3}$. These simulations

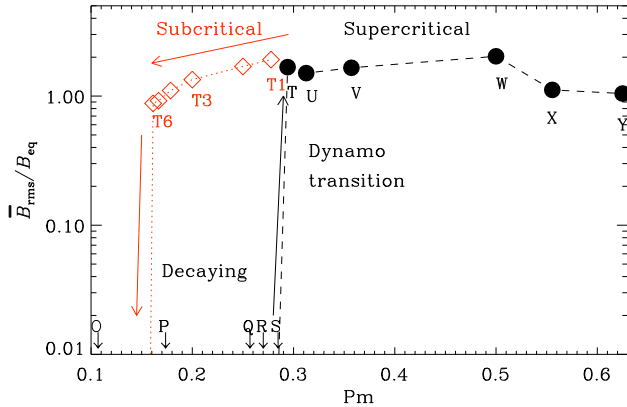


FIG. 5.— Similar to Figure 1 but from a different set of simulations (Set II) where η is varied while σ and ν are held fixed (Runs N–T12).

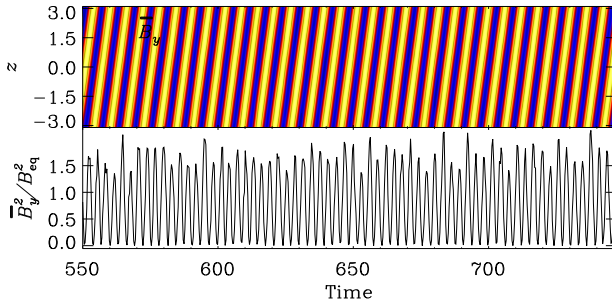


FIG. 6.— In the bistable dynamo state of Figure 5: The simulation started from strong initial field at $P_m = 0.1613$, just before the decaying solution (Run T6). The format is the same as Figure 2.

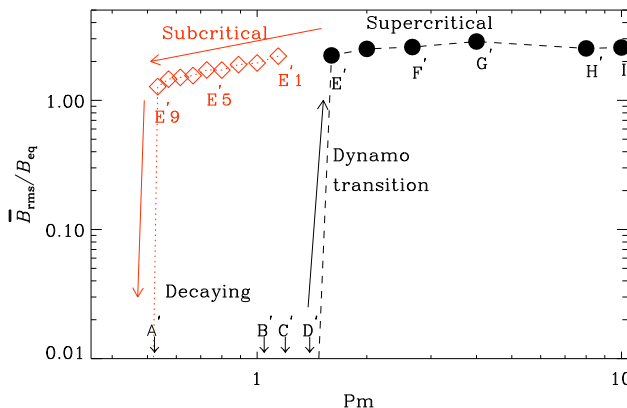


FIG. 7.— Similar to Figure 5 but simulations are performed at $k_f = 3$ and $\nu = 8 \times 10^{-3}$ (Set III in Table 2).

are at slightly higher R_m . Table 2 gives a summary of these runs, and Figure 7 shows the corresponding dynamo hysteresis. We clearly see a similar behavior.

4. COMPARISON WITH ANALYTIC PREDICTIONS

To understand why the hysteresis discussed in this paper has not been seen before, we need to assess more carefully the parameter regimes of our solutions. Given that we use (shearing-) periodic boundary conditions, there are no magnetic helicity fluxes in or out of the domain, so

TABLE 2
SAME AS SET II IN TABLE 1 BUT SIMULATIONS ARE PERFORMED AT FORCING WAVENUMBER $k_f = 3$ AND $\nu = 8 \times 10^{-3}$.

Set III								
Run	P_m	u_{rms}	R_m	D	\bar{B}	\bar{B}_x	\bar{B}_y	Osc
A'	0.50	0.28	5.5	2.63	0.00	0.00	0.00	N
B'	1.00	0.38	15.0	1.71	0.00	0.00	0.00	N
C'	1.14	0.38	17.4	1.76	0.00	0.00	0.00	N
D'	1.33	0.32	17.2	2.77	0.00	0.00	0.00	N
E'	1.60	0.14	9.1	14.81	2.23	0.19	2.08	Y
F'	2.00	0.13	10.8	18.66	2.50	0.19	2.39	Y
G'	2.67	0.13	14.0	23.13	2.59	0.18	2.36	Y
H'	4.00	0.13	21.3	25.01	2.85	0.15	2.63	Y
I'	8.00	0.13	42.6	29.19	2.52	0.12	2.25	Y
E'1	1.14	0.13	6.0	13.99	2.20	0.22	2.09	Y
E'2	1.00	0.14	5.5	11.15	1.95	0.21	1.85	Y
E'3	0.89	0.14	4.8	10.74	1.89	0.22	1.80	Y
E'4	0.80	0.15	4.7	8.36	1.72	0.21	1.61	Y
E'5	0.73	0.14	4.0	8.79	1.72	0.22	1.64	Y
E'6	0.67	0.15	3.9	7.44	1.56	0.21	1.48	Y
E'7	0.62	0.14	3.4	7.59	1.51	0.22	1.43	Y
E'8	0.57	0.14	3.1	7.48	1.46	0.22	1.36	Y
E'9	0.53	0.15	3.2	5.64	1.28	0.21	1.23	Y
E'10	0.50	0.36	7.2	1.36	0.00	0.00	0.00	Y

we can describe the solutions by comparing with the analytic results of Blackman & Brandenburg (2002, hereafter BB02). The dynamical quenching theory used in BB02 was already compared with numerical solutions by Käpylä & Brandenburg (2009). One of the predictions they tested was that the saturation level of the mean magnetic field, which they gave in the form

$$\frac{B_{\text{rms}}^2}{B_{\text{eq}}^2} \approx \frac{\epsilon_f k_f}{\epsilon_m k_m} - \left(1 + \frac{\eta}{\eta_{t0}}\right), \quad (8)$$

where k_f and k_m are respectively the effective wavenumbers of the fluctuating and mean fields, defined via $k_f^2 = \langle \mathbf{j} \cdot \mathbf{b} \rangle / \langle \mathbf{a} \cdot \mathbf{b} \rangle$ and $k_m^2 = \langle \bar{\mathbf{J}} \cdot \bar{\mathbf{B}} \rangle / \langle \bar{\mathbf{A}} \cdot \bar{\mathbf{B}} \rangle$, and ϵ_f and ϵ_m are their fractional helicities, defined via

$$\epsilon_f k_f = \mu_0 \langle \mathbf{j} \cdot \mathbf{b} \rangle / \langle \mathbf{b}^2 \rangle, \quad \epsilon_m k_m = \mu_0 \langle \bar{\mathbf{J}} \cdot \bar{\mathbf{B}} \rangle / \langle \bar{\mathbf{B}}^2 \rangle. \quad (9)$$

Figure 8 shows our data from two sets of simulations (Sets I–II) which produce significant large-scale magnetic fields. We have added labels on some of the data to identify the runs. We note that, unlike Figures 1 and 5, where we have plotted $\bar{B}_{\text{rms}}/B_{\text{eq}}$, here we plot $\bar{B}_{\text{rms}}/B_{\text{eq}}^2$, but in a smaller range which is why the data in Figure 8 show a nearly linear variation. Even in a limited range, apart from a small offset, there is a reasonable agreement between our data and the theory (Equation (8); dotted line). However, Käpylä & Brandenburg (2009) had data in a wider range and found better agreement for higher field strengths. In Figure 8 we observe that, when increasing the helicity parameter σ (from Runs E to M in Set I), both the wavenumber ratio of fluctuating to mean fields, as defined by Equation (9), and the mean field strength decrease. A similar trend is followed while decreasing σ (Runs E1–E8), except for the last few runs (Runs E9–E11), which deviate significantly. Qualitatively similar behavior is observed in Set II, when P_m is decreased from Runs T1 to T6, although they consistently deviate from the other runs. However for Runs T–Z, the trend is not monotonous.

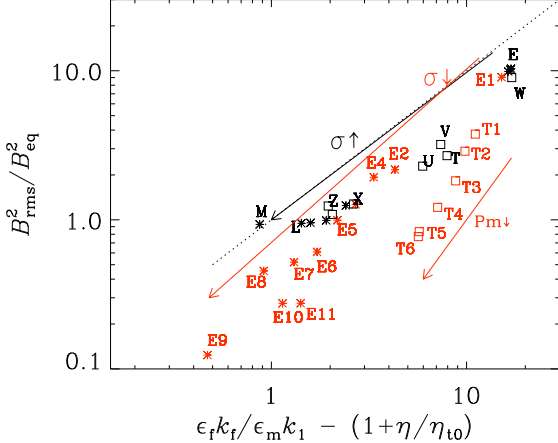


FIG. 8.— Scatter plot between $\overline{B}^2_{\text{rms}}/B_{\text{eq}}^2$ and $\epsilon_F k_F/\epsilon_m k_1 - (1 + \eta/\eta_{\text{to}})$. Dotted line shows the comparison with theory. The black asterisks represent data from Runs E–M of Set I (also represented by black points in Figure 1), whereas red asterisks are from Runs E1–E11 (red points in Figure 1). The black squares represent data from Runs T–Z of Set II (also represented by black points in Figure 5), whereas red squares are from Runs T1–T6 (red points in Figure 5).

Another prediction of BB02 was that ϵ_m is directly proportional to the ratio of poloidal to toroidal magnetic field amplitudes via

$$\epsilon_m = \left(2\langle \bar{B}_x^2 \rangle / \langle \bar{B}_y^2 \rangle \right)^{1/2}. \quad (10)$$

From Equation (9) we compute ϵ_m by assuming $k_m = -k_1$ and show in Figure 9 a scatter plot of ϵ_m vs. $(2\langle \bar{B}_x^2 \rangle / \langle \bar{B}_y^2 \rangle)^{1/2}$. Here we see better agreement with Equation (10) indicated by the dotted line. In Set I, with increasing σ from Runs E to M, the ratio of poloidal to toroidal field increases, but the same happens from Runs E1 to E11 with decreasing σ as well, which was unexpected. The same trend is observed as we decrease P_m from Runs T1 to T6 in Set II, but in Runs T-Z the variation is not monotonous. Furthermore, we note that the data points corresponding to two different regimes—subcritical and supercritical—lie on different lines (compare red and black points in Figure 9).

We notice that in Figure 8, and also to some extent in Figure 9, the simulation data are systematically below the analytically expected values. A smaller value of $\overline{B}_{\text{rms}}$ could readily be explained as being a combination of several modes, which results in reduced averages. This is reminiscent of the fratricide $\alpha\Omega$ dynamos of Hubbard et al. (2011), who found that they can be destroyed by their growing α^2 dynamo siblings. An important difference, however, is that they never found the recovery of the $\alpha\Omega$ dynamo. This might be related to the close proximity of dynamo onset.

5. CONCLUSION AND DISCUSSION

As discussed in the Introduction, dynamo hysteresis predicted by the nonlinear mean-field model of Kitchatinov & Olemskoy (2010) may be relevant to the understanding of distinct modes of solar activity found by Usoskin et al. (2014). Our simulations of turbulent

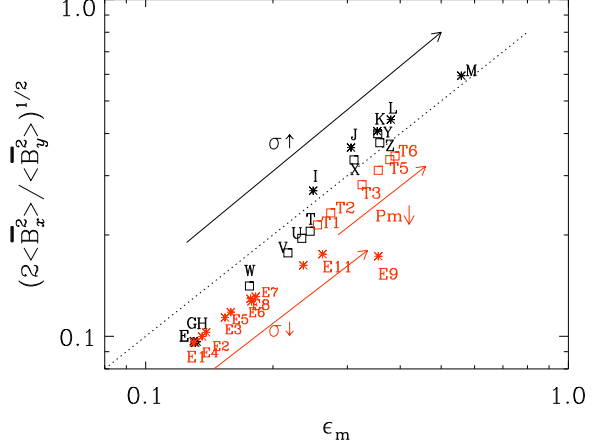


FIG. 9.— Scatter plot between the ratio of the poloidal to toroidal field and ϵ_m . Dotted line shows the comparison with theory. Representation of data symbol are same as in Figure 8.

dynamics in shearing boxes with helically forced turbulent flows, which resemble the equivalent $\alpha\Omega$ solar dynamo, demonstrate, for the first time, hysteresis behavior. By performing several simulations, either by varying the helicity parameter σ or the magnetic Prandtl number P_m , we observe two stable states with largely different characteristic field strengths depending on the initial conditions of the simulation. A decaying solution is obtained when the simulation is started with weak random seed fields, but otherwise an oscillatory solution is obtained when the simulation is started from a snapshot of a previous oscillatory dynamo.

We emphasize that our simulations show hysteresis close to dynamo onset only. This raises the question of whether the Sun may be close to the marginal state for the dynamo. Stellar observations indicate that this might indeed be the case. Magnetic activity is known to be correlated with rotation rate, but leads to angular momentum loss through a magnetically coupled stellar wind (Kraft 1967; Hartmann & Noyes 1987). Spin-down of solar-type stars does not continue above a certain rotation period that depends on the spectral type (Rengarajan 1984). The maximum period probably corresponds to the rotation rate where the global dynamo ceases. The maximum period for G2 dwarfs is only slightly larger than the rotation period of the Sun (see Fig. 1 in Rengarajan 1984). The stars showing low magnetic activity similar to the solar grand minima are typically old and slow rotators (Saar & Baliunas 1992).

The dynamo hysteresis, however, is not needed for interpreting distinct modes of solar activity. It is only necessary that dynamo modes with largely different field strengths are present in close vicinity of the dynamo threshold. In our simulations, the distinct dynamo modes were, however, accompanied by hysteresis. Fluctuations in small-scale flows are inherent to 3D simulations and may cause transitions between the distinct dynamo regimes. The transitions do indeed happen in the simulations with relative kinetic helicity below unity (Figure 4). The intermittency of distinct dynamo regimes, however, disappeared for maximally helical forcing (Figure 6), which would not be realistic for the Sun

anyway. Dependence of the intermittency on the (fractional) helicity remains to be explored.

Besides the demonstration of a hysteresis phenomenon in a turbulent dynamo, we have analyzed the simulation data to compare with the dynamical theory of BB02. We observe that the data from subcritical and supercritical dynamos behave in a qualitatively similar way and that they are in reasonable agreement with the theoretical predictions. We end by remarking that, although our findings of hysteresis between two distinct modes of dynamos is relevant to the recently discovered bi-modal solar activity of Usoskin et al. (2014), our simulations are far from the real Sun. Therefore, future research is necessary to explore similar behaviors in more realistic

setups.

LLK is thankful to the Russian Foundation for Basic Research (project 13-02-00277) for the support and AB acknowledges support through the Swedish Research Council grants 621-2011-5076 and 2012-5797, the Research Council of Norway under the FRINATEK grant 231444. The computations have been carried out at the National Supercomputer Centres in Linköping and Umeå, the Center for Parallel Computers at the Royal Institute of Technology in Sweden, and the Nordic High Performance Computing Center in Iceland.

REFERENCES

- Blackman, E. G., & Brandenburg, A. 2002, *ApJ*, 579, 359
 Brandenburg, A., & Guerrero, G. 2012, in IAU Symposium, Vol. 286, IAU Symposium, ed. C. H. Mandrini & D. F. Webb, 37–48
 Brandenburg, A., & Spiegel, E. A. 2008, *Astron. Nachr.*, 329, 351
 Charbonneau, P., Blais-Laurier, G., & St-Jean, C. 2004, *ApJ*, 616, L183
 Choudhuri, A. R. 1992, *A&A*, 253, 277
 Choudhuri, A. R., & Karak, B. B. 2009, *Res. Astron. Astrophys.*, 9, 953
 —. 2012, *Physical Review Letters*, 109, 171103
 Hartmann, L. W., & Noyes, R. W. 1987, *ARA&A*, 25, 271
 Haugen, N. E., Brandenburg, A., & Dobler, W. 2004, *Phys. Rev. E*, 70, 016308
 Hoyt, D. V., & Schatten, K. H. 1996, *Sol. Phys.*, 165, 181
 Hubbard, A., Rheinhardt, M., & Brandenburg, A. 2011, *A&A*, 535, A48
 Käpylä, P. J., & Brandenburg, A. 2009, *ApJ*, 699, 1059
 Karak, B. B. 2010, *ApJ*, 724, 1021
 Karak, B. B., & Choudhuri, A. R. 2013, *Res. Astron. Astrophys.*, 13, 1339
 Karak, B. B., Käpylä, P. J., Käpylä, M. J., & Brandenburg, A. 2014, arXiv:1407.0984
 Kitchatinov, L. L., & Olemskoy, S. V. 2010, *Astronomy Letters*, 36, 292
 Kraft, R. P. 1967, *ApJ*, 150, 551
 Krause, F., & Rädler, K. H. 1980, *Mean-field magnetohydrodynamics and dynamo theory* (Oxford: Pergamon Press)
 Moss, D., Sokoloff, D., Usoskin, I., & Tutubalin, V. 2008, *Sol. Phys.*, 250, 221
 Nelson, N. J., Brown, B. P., Brun, A. S., Miesch, M. S., & Toomre, J. 2013, *ApJ*, 762, 73
 Olemskoy, S. V., & Kitchatinov, L. L. 2013, *ApJ*, 777, 71
 Ossendrijver, A. J. H., Hoyng, P., & Schmitt, D. 1996, *A&A*, 313, 938
 Passos, D., Nandy, D., Hazra, S., & Lopes, I. 2014, *A&A*, 563, A18
 Rempel, E. L., Proctor, M. R. E., & Chian, A. C.-L. 2009, *MNRAS*, 400, 509
 Rengarajan, T. N. 1984, *ApJ*, 283, L63
 Rüdiger, G., Kitchatinov, L. L., Küker, M., & Schultz, M. 1994, *Geophysical and Astrophysical Fluid Dynamics*, 78, 247
 Saar, S. H., & Baliunas, S. L. 1992, in *Astronomical Society of the Pacific Conference Series*, Vol. 27, *The Solar Cycle*, ed. K. L. Harvey, 150–167
 Usoskin, I. G., Solanki, S. K., & Kovaltsov, G. A. 2007, *A&A*, 471, 301
 Usoskin, I. G., et al. 2014, *A&A*, 562, L10